

# Constructing CO-immune water dissociation sites around Pt to achieve stable operation in high CO concentration environment

Received: 3 September 2023

Accepted: 6 August 2024

Published online: 16 September 2024

Check for updates

Daojun Long<sup>1,3</sup>, Yongduo Liu<sup>1,3</sup>, Xinyu Ping<sup>1</sup>, Fadong Chen<sup>1</sup>, Xiongxin Tao<sup>1</sup>, Zhenyang Xie<sup>1</sup>, Minjian Wang<sup>1</sup>, Meng Wang<sup>1</sup>, Li Li<sup>1</sup>, Lin Guo<sup>2</sup>✉, Siguo Chen<sup>1</sup>✉ & Zidong Wei<sup>1</sup>

The serious problem of carbon monoxide (CO) poisoning on the surface of Pt-based catalysts has long constrained the commercialization of proton exchange membrane fuel cells (PEMFCs). Regeneration of Pt sites by maintaining CO scavenging ability through precise construction of the surface and interface structure of the catalyst is the key to obtaining high-performance CO-resistant catalysts. Here, we used molybdenum carbide (MoC<sub>x</sub>) as the support for Pt and introduced Ru single atoms (SA-Ru) at the Pt-MoC<sub>x</sub> interface to jointly decrease the CO adsorption strength on Pt. More importantly, the MoC<sub>x</sub> and SA-Ru are immune to CO poisoning, which continuously assists in the oxidation of adsorbed CO by generating oxygen species from water dissociation. These two effects combine to confer this anode catalyst (SA-Ru@Pt/MoC<sub>x</sub>) remarkable CO tolerance and the ability to operate stably in fuel cell with high CO concentration (power output 85.5 mW cm<sup>-2</sup>@20,000 ppm CO + H<sub>2</sub> - O<sub>2</sub>), making it possible to directly use the cheap reformed hydrogen as the fuel for PEMFCs.

Proton exchange membrane fuel cells (PEMFCs) are recognized as one of the most promising alternatives to diesel engines for heavy-duty trucking and military applications<sup>1</sup>. In order to reduce the running cost of PEMFCs to promote its commercialization, the cheap and scalable H<sub>2</sub> (≈US\$ 1.5 kg<sup>-1</sup>) from coal gasification and methane reforming is widely recognized as an alternative fuel to pure H<sub>2</sub><sup>2-5</sup> (>US\$ 13 kg<sup>-1</sup> in the market). However, the common Pt-based hydrogen oxidation reaction (HOR) catalysts for PEMFCs are easily poisoned by CO (1–3%) contained in reformed gas, resulting in a rapid decrease in the output power density of PEMFCs<sup>6-9</sup>. Even after CO purification by costly selective oxidation or membrane separation, the remaining trace amount of CO (10 ppm) can still deactivate the state-of-the-art Pt/C catalyst, which can hardly meet the long-term durability requirements for PEMFCs<sup>10-12</sup>. Therefore, improving the CO tolerance of Pt is of great importance.

The reason why Pt-based catalysts are severely affected by CO is that, in addition to the strong adsorption of CO on the Pt surface, the Pt surface requires a high overpotential (0.7–0.9 V vs. RHE) that far beyond the HOR equilibrium potential (0 V vs. RHE) to dissociate water to produce OH for oxidizing CO<sup>13</sup>. Therefore, reducing the adsorption strength of CO and introducing hydrolysis sites around Pt to generate OH (bifunctional mechanism) is the mainstream approach in this issue<sup>14-17</sup>. According to the Blyholder model, the chemical bond between adsorbed CO (CO<sub>ads</sub>) and Pt mainly originates from the combination of electron donation from the CO 5σ orbital to the metal d orbital (5d<sub>z<sup>2</sup></sub>) and metal d-electron (d<sub>xz</sub> or d<sub>yz</sub>) back-donation to the CO 2π\* antibonding orbital<sup>18,19</sup>. Therefore, focused modulation of the d-electronic structure of Pt is an effective way to attenuate CO adsorption<sup>20-24</sup>. In recent years, the CO tolerant performance of catalysts has been effectively improved by decreasing the d-band center of

<sup>1</sup>College of Chemistry and Chemical Engineering, State Key Laboratory of Advanced Chemical Power Sources (SKL-ACPS), Chongqing University, Chongqing, China. <sup>2</sup>Research Institute of Petroleum Processing Co., Ltd., SINOPEC, Beijing, China. <sup>3</sup>These authors contributed equally: Daojun Long, Yongduo Liu. ✉e-mail: [guolin.ripp@sinopec.com](mailto:guolin.ripp@sinopec.com); [csg810519@126.com](mailto:csg810519@126.com)

Pt through strategies such as introducing transition metals to form alloys, preparing core-shell structures, and using oxide supports, which attenuates the electronic feedback from Pt to CO<sub>ads</sub><sup>25–29</sup>. Xing et al. fabricated Pt<sub>6</sub> nanoclusters with an apparently downshifted d-band center compared to Pt single atom and Pt nanoparticles, which showed a weakened CO adsorption<sup>30</sup>. Zhang et al. used CrN as the support to modulate the electronic structure of Pt and made the Pt in an oxidation state (Pt<sup>δ+</sup>), which resulted in a lower filling of the Pt d-band and reduced electron back-donation to CO 2π<sup>\*31</sup>. Similarly, the non-precious metal catalyst Co-MoNi reported by Gao et al. reduces the d-band center of Ni and thus weakens the adsorption of CO molecules by the same strategies as above<sup>21</sup>. So far, the best anti-CO Pt-based catalyst recognized is the commercial PtRu/C, which not only effectively reduces the d-band center of Pt due to alloying with Ru, but also Ru as an oxyphilic site can dissociate water and release –OH to help the oxidation of CO on the Pt surface<sup>4,32</sup>. Unfortunately, this promising catalyst, as well as most of the catalysts reported in the literature, are not yet able to operate sustainably with H<sub>2</sub> containing high concentrations of CO (>1000 ppm). This is due to the fact that CO adsorption can only be attenuated, not completely inhibited, and the Pt active site is still slowly poisoned under fuel cell operating conditions (Fig. 1a). More importantly, and often overlooked, is that the –OH generating site, Ru can be severely poisoned<sup>33–37</sup>. Therefore, in addition to modulating the electronic structure of Pt-based catalysts to attenuate CO adsorption, it is necessary to construct water dissociation sites that are immune to CO poisoning to ensure a continuous supply of –OH to aid in the regeneration of active sites.

Here, we synthesized a model catalyst capable of spontaneous regeneration of active sites using molybdenum carbide as a support for Pt clusters combined with a strategy of surface Ru single-atoms (SA-Ru) modification. In this structure, there happens a strong metal support interaction between MoC<sub>x</sub> and Pt, which can lower the d-band center of Pt and reduce the electron backdonation from Pt to CO<sub>ads</sub>. In addition, the MoC<sub>x</sub> surface is very easily hydroxylated to form surface \*OH to help remove CO impurities from H<sub>2</sub> (Fig. 1b). The introduction of SA-Ru further reduces the adsorption strength of CO on the Pt cluster surface, and the SA-Ru at the interface of MoC<sub>x</sub>-Pt NPs could not be poisoned by CO, which can continue to serve as the dissociation site of water to provide –OH in the CO-containing environment. These

advantages endow the SA-Ru@Pt/MoC<sub>x</sub> catalyst high CO tolerance and the ability to operate stably in an environment with high CO concentrations.

## Results and discussion

The SA-Ru@Pt/MoC<sub>x</sub> catalyst was prepared by heating the dual-shell SiO<sub>2</sub>@PDA-Ru<sup>3+</sup>@Pt/MoO<sub>3</sub> precursor at 700 °C in H<sub>2</sub>/N<sub>2</sub> (1:9) for 2 h (Supplementary Fig. 1). The outer SiO<sub>2</sub> shell isolated a confined space to prevent sintering of the Pt particles during the heat treatment. The inner polydopamine (PDA) shell was served as the carbon source for the conversion of MoO<sub>3</sub> to MoC<sub>x</sub> and the function of homogeneous absorption of Ru<sup>3+</sup>. During the high temperature annealing, the former Pt nanoparticles (NPs) on MoO<sub>3</sub> broke up into smaller Pt clusters and Ru<sup>3+</sup> was reduced to SA-Ru in the vicinity of Pt by H<sub>2</sub>. The structural evolution from Pt/MoO<sub>3</sub> to SA-Ru@Pt/MoC<sub>x</sub> was first investigated by transmission electron microscopy (TEM) and X-ray diffraction (XRD) experiments (Fig. 2 and Supplementary Fig. 2). The TEM image and corresponding energy dispersive X-ray (EDX) mappings of Pt/MoO<sub>3</sub> show that the initial Pt NPs with an average size of 4.28 nm were dispersed on the surface of the MoO<sub>3</sub> substrate (Fig. 2a–e and Supplementary Fig. 3). After annealing, the XRD peaks of MoO<sub>3</sub> in the precursor (Pt/MoO<sub>3</sub>) disappeared and were replaced by a couple of MoC<sub>x</sub> peaks at 36.4° and 42.3° (PDF#89-2868), indicating the successful carbonization of MoO<sub>3</sub> by PDA pyrolysis. Interestingly, the peaks of Pt in Pt/MoO<sub>3</sub> and SA-Ru@Pt/MoC<sub>x</sub> were not changed and agreed well with the PDF card of pure Pt (JCPDS: 87-0640), indicating that the Pt was not alloyed with Ru or Mo after annealing. Further aberration-corrected high-angle annular dark-field scanning transmission electron microscopy (HAADF-STEM) images and EDX mapping show that thermal annealing of SiO<sub>2</sub>@PDA-Ru<sup>3+</sup>@Pt/MoO<sub>3</sub> leads to redispersion of Pt NPs into smaller Pt clusters (2 nm) surrounded by large amounts of single atoms with brighter contrast (Fig. 2g and Supplementary Figs. 4 and 5). The formation of smaller Pt clusters is attributed to the anti-Ostwald effect, in which the surface Pt atoms of Pt NPs were emitted outward by thermal motion under high temperature, and the mobile Pt atoms could subsequently be captured by MoC<sub>x</sub> through covalent interaction<sup>38,39</sup>. This assertion was confirmed by comparing the EDX mapping before and after annealing (Fig. 2h–k), where the isolated Pt NPs signal in Pt/MoO<sub>3</sub> was changed to dispersion

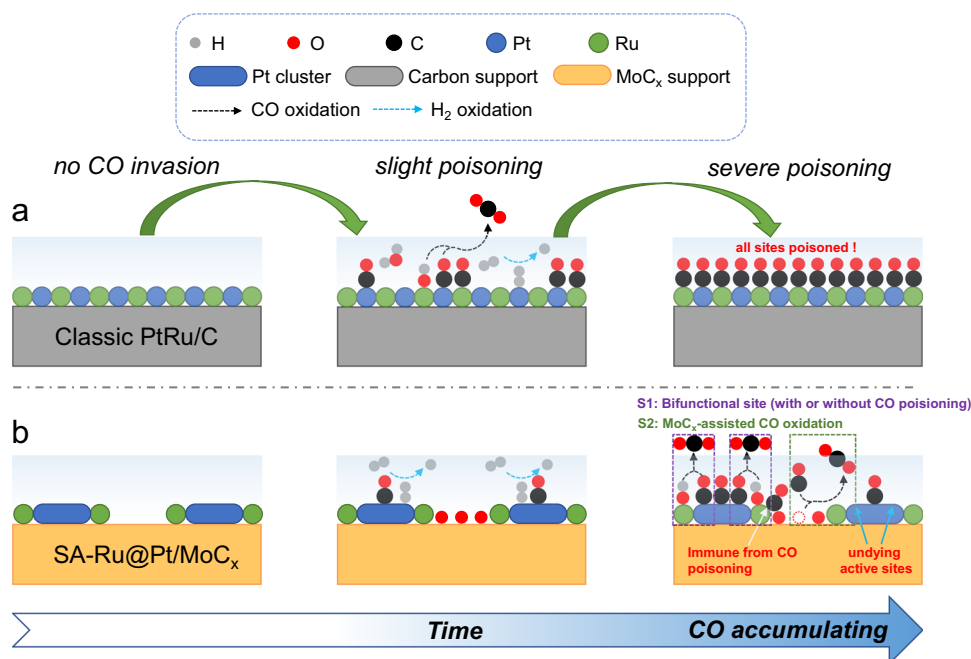


**Fig. 1** | Schematic diagram of the CO poisoning and removal process on different catalysts. **a** PtRu; **b** SA-Ru@Pt/MoC<sub>x</sub>.

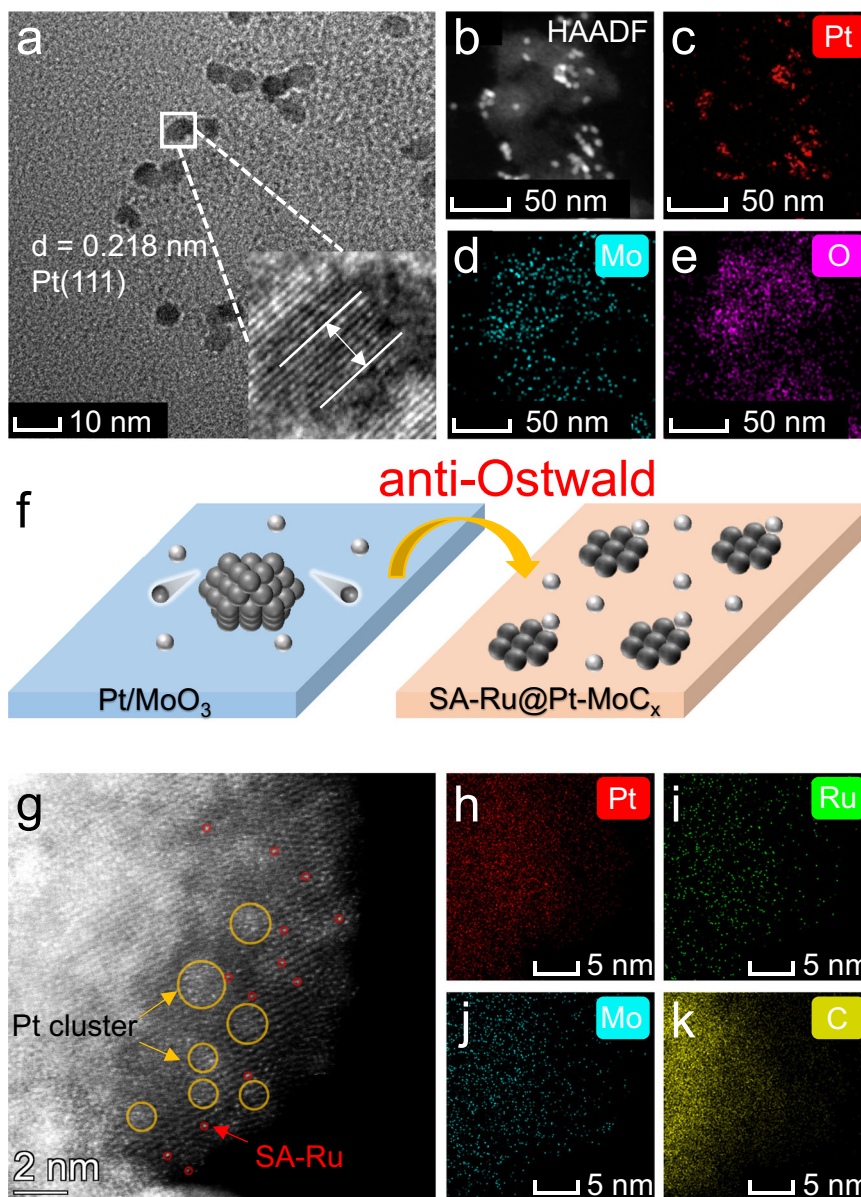


**Fig. 2 | Physical structure characterizations of Pt/MoO<sub>3</sub> and SA-Ru@Pt/MoC<sub>x</sub>.** **a, b** TEM and HAADF image of the initial Pt/MoO<sub>3</sub>. **c–e** Corresponding EDX elementary mapping of Pt/MoO<sub>3</sub>. **f** Illustration of the formation mechanism of SA-

Ru@Pt/MoC<sub>x</sub>. **g** High-resolution HAADF-STEM image of SA-Ru@Pt/MoC<sub>x</sub>. **h–k** Corresponding elemental mappings of SA-Ru@Pt/MoC<sub>x</sub>.

style on the MoC<sub>x</sub> substrate of SA-Ru@Pt/MoC<sub>x</sub>. Noticing that the EDX signal of Ru was homogeneously distributed in the observation zone (Fig. 2i and Supplementary Fig. 6) and combined with the absence of Ru characteristic peaks in the SA-Ru@Pt/MoC<sub>x</sub> XRD pattern, we deduce that most of the spots with bright contrast spreading around Pt clusters are Ru single atoms. Since Pt has a higher Z-number than Ru, thus we cannot exclude that some of the bright atoms are Pt single atoms that produced by the anti-Ostwald effect. This speculation was further discussed in the following spectral characterization.

The extended X-ray absorption fine structure (EXAFS) was used to reveal the chemical environment of the three metal elements in SA-Ru@Pt/MoC<sub>x</sub>. Due to the number of fitted variables (e.g., Pt-Pt, Pt-Ru, Pt-Mo, metal-O bonds) is close to that of independent points, the fitting process has a low degree of freedom. We used FEFF calculations to delineate the peaks in the R-space of SA-Ru@Pt/MoC<sub>x</sub> (Supplementary Fig. 9 and Table 5). There's a new strong peak located at 2.2 Å in the R space of Pt, which indicates the strong interaction between Pt and MoC<sub>x</sub> support<sup>40</sup> (Fig. 3a). In alignment with EXAFS result, the wavelet

transform (WT) image of Pt shows the obvious Pt-Pt scattering path at 12.9 Å<sup>-1</sup> and another intensity maxima at 8.1 Å<sup>-1</sup> for Pt-Mo/Ru path (Fig. 3d). While, the R-space scattering path of Pt does not exhibit the characteristic peaks of the Pt single atoms. Therefore, even if Pt single atoms are present, they should be in very small amounts. The presence of Mo-Pt bonds was also demonstrated by the peak signal at 2.69 Å in the R space and at 11.9 Å<sup>-1</sup> in the WT image of Mo<sup>41</sup> (Fig. 3b, e). The strong Mo-Pt bond indicates the existence of PtMo clusters, which could be the amorphous PtMo mixture that was not detected by XRD. And the shoulder peak at 2.43 Å could be assigned to the Mo-Ru pathway with the corresponding peak at 10.1 Å<sup>-1</sup> in the WT image<sup>42</sup>. The scattering path of Ru shows a distinct peak at 1.6 Å and the WT image of Ru shows a strong signal at 5.5 Å<sup>-1</sup>, indicating that a considerable amount of Ru coordinates with C/N/O to form Ru single atoms<sup>43–45</sup> (Fig. 3c, f). Thus, combining the Ru bonding character, XRD results and EDX mapping, most of the single atoms observed in STEM should be Ru. However, it should be noted that there are still coordination peaks of Ru with Mo/Ru and Pt still at positions 2.24 Å and 2.70 Å,



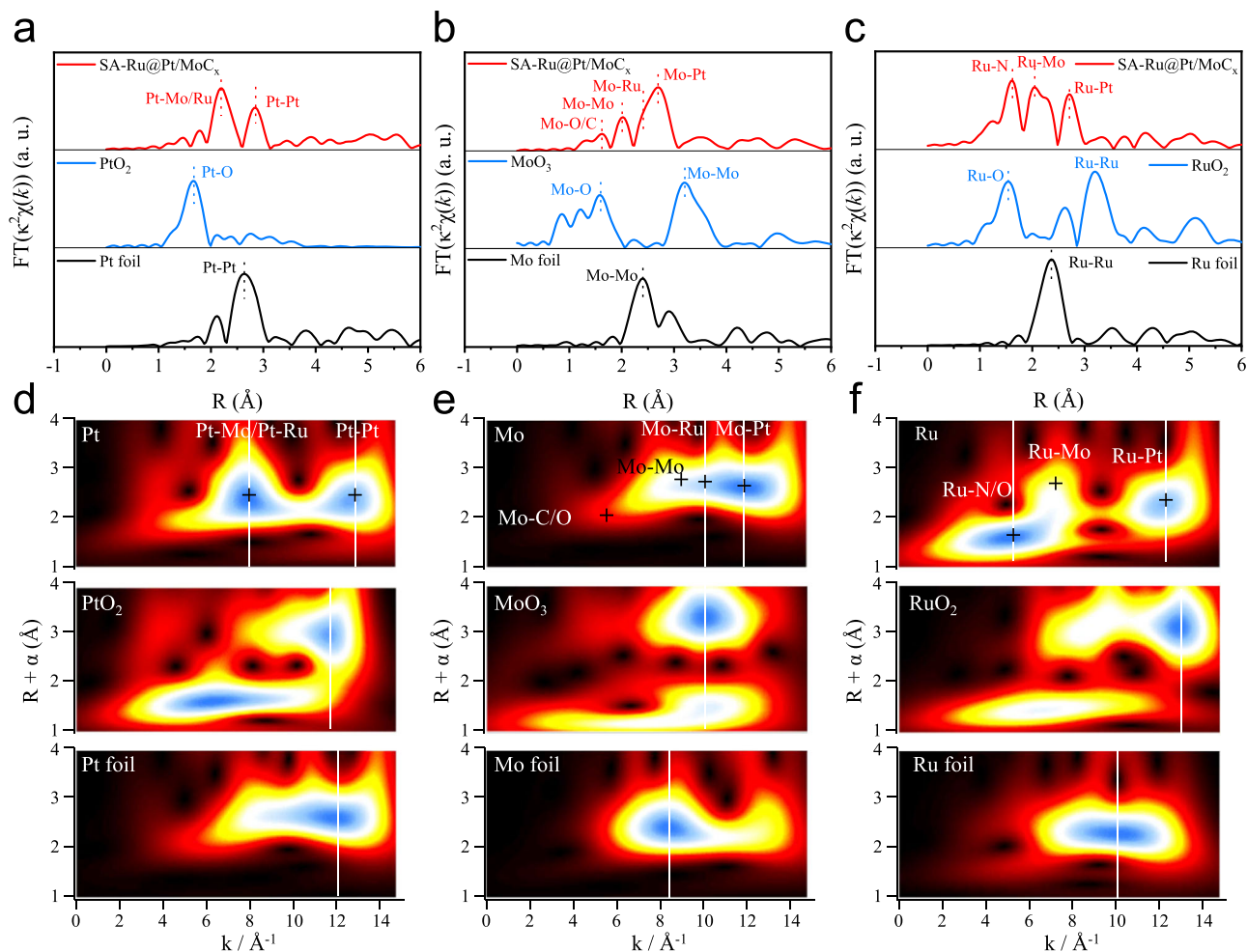


**Fig. 3 | Coordination environments characterizations.** **a–c** Fourier transformed  $k^3$ -weighted  $\chi(k)$ -function of the EXAFS spectra for Pt  $L_3$ -edge, Mo K-edge and Ru K-edge. **d–f** Corresponding wavelet transforms for the  $k^3$ -weighted EXAFS of Pt, Mo and Ru.

respectively<sup>46,47</sup>. Excluding the presence of SA-Ru on the surface of Pt and  $\text{MoC}_x$ , this is related to the coexistence of amorphous blocks that composed of Pt, Mo and Ru, which are formed by particle sintering in the current synthesis method (Supplementary Fig. 7).

The strong interaction between Pt and Mo has significantly changed the electronic structure of Pt in SA-Ru@Pt/MoC<sub>x</sub><sup>48,49</sup>. This was observed by an increase in the “white line” intensity of SA-Ru@Pt/MoC<sub>x</sub> compared to Pt foil in the X-ray absorption near edge structure (XANES) (Fig. 4a and Supplementary Fig. 10a, b). The electron-deficient state of Pt in SA-Ru@Pt/MoC<sub>x</sub> was also confirmed by the 0.21 eV positive shift of the Pt 4f binding energy in X-ray photoelectron spectroscopy (XPS) with respect to Pt/C, due to the electron transfer from Pt to the MoC<sub>x</sub> substrate (Fig. 4d and Supplementary Fig. 21). As mentioned above, this type of electron-deficient state is beneficial to reduce the electron backdonation from Pt to CO<sub>ads</sub>, which further reduces CO adsorption<sup>20,50</sup>. The valence of Mo was reduced by carbonization, as evidenced by the adsorption edge of Mo located in the middle of the Mo foil and MoO<sub>3</sub> (Fig. 4b and Supplementary Fig. 10c, d). And the appearance of a new peak at 228.3 eV in Mo high-resolution XPS spectroscopy indicates the formation of MoC<sub>x</sub> (Fig. 4e). As can be seen in Fig. 4c, f and Supplementary Fig. 10e, f, the K-edge XANES and high resolution XPS spectra indicate that the chemical state of Ru is partially oxidized due to its tendency to dissociate H<sub>2</sub>O from environment, which is beneficial to spontaneously provide -OH for CO<sub>ads</sub> oxidation on Pt in working environment<sup>51,52</sup>.

The HOR activity and CO tolerance of SA-Ru@Pt/MoC<sub>x</sub> were evaluated in an aqueous electrochemical test. SA-Ru@Pt/MoC<sub>x</sub> and

commercial PtRu/C showed a similar limiting diffusion current density ( $J_d$ ) of 2.75 mA cm<sup>-2</sup> in pure H<sub>2</sub> saturated HClO<sub>4</sub> (Supplementary Fig. 13). After changing the solution to 0.1M HClO<sub>4</sub> saturated with 20,000 ppm CO/H<sub>2</sub> mixture, the  $J_d$  of SA-Ru@Pt/MoC<sub>x</sub> decreased by 7.1% as compared to the value in pure H<sub>2</sub>, which is lower than that of commercial PtRu/C (11.8%). The catalytic stability in CO containing environment was further examined by chronoamperometric method in H<sub>2</sub> + 20,000 ppm CO saturated solution (Supplementary Fig. 14). The HOR current density of commercial PtRu/C showed a continuous decrease and finally dropped to zero within 550 s. While the HOR current density of SA-Ru@Pt/MoC<sub>x</sub> only slightly decreased by 12.2% compared to the situation of pure H<sub>2</sub>. The above results prove that the CO tolerance of SA-Ru@Pt/MoC<sub>x</sub> is higher than commercial PtRu/C in aqueous environment.

To simulate the realistic working environment in PEMFC, the performance of SA-Ru@Pt/MoC<sub>x</sub>-based MEA was tested using standard H<sub>2</sub>/CO mixture as anode fuel with commercial PtRu/C as a benchmark for comparison (the JM Pt/C was used as cathode and all the Pt loading is 0.1 mg cm<sup>-2</sup>). As shown in Fig. 5a, d, the SA-Ru@Pt/MoC<sub>x</sub> based MEA under H<sub>2</sub>-O<sub>2</sub> condition exhibits lower peak power density (610 mW cm<sup>-2</sup>) than the commercial PtRu/C single cell (1200 mW cm<sup>-2</sup>). This is due to the presence of large metal blocks in the current synthesis method, resulting in the low specific surface area of SA-Ru@Pt/MoC<sub>x</sub> (Supplementary Figs. 7 and 15 and Table 6). When the anode gas was changed to H<sub>2</sub> + 10,000 ppm CO, the peak power density of PtRu/C-based MEA dropped by nearly 96.7% (40 mW cm<sup>-2</sup>) relative to the initial output power in pure H<sub>2</sub> condition only after 5

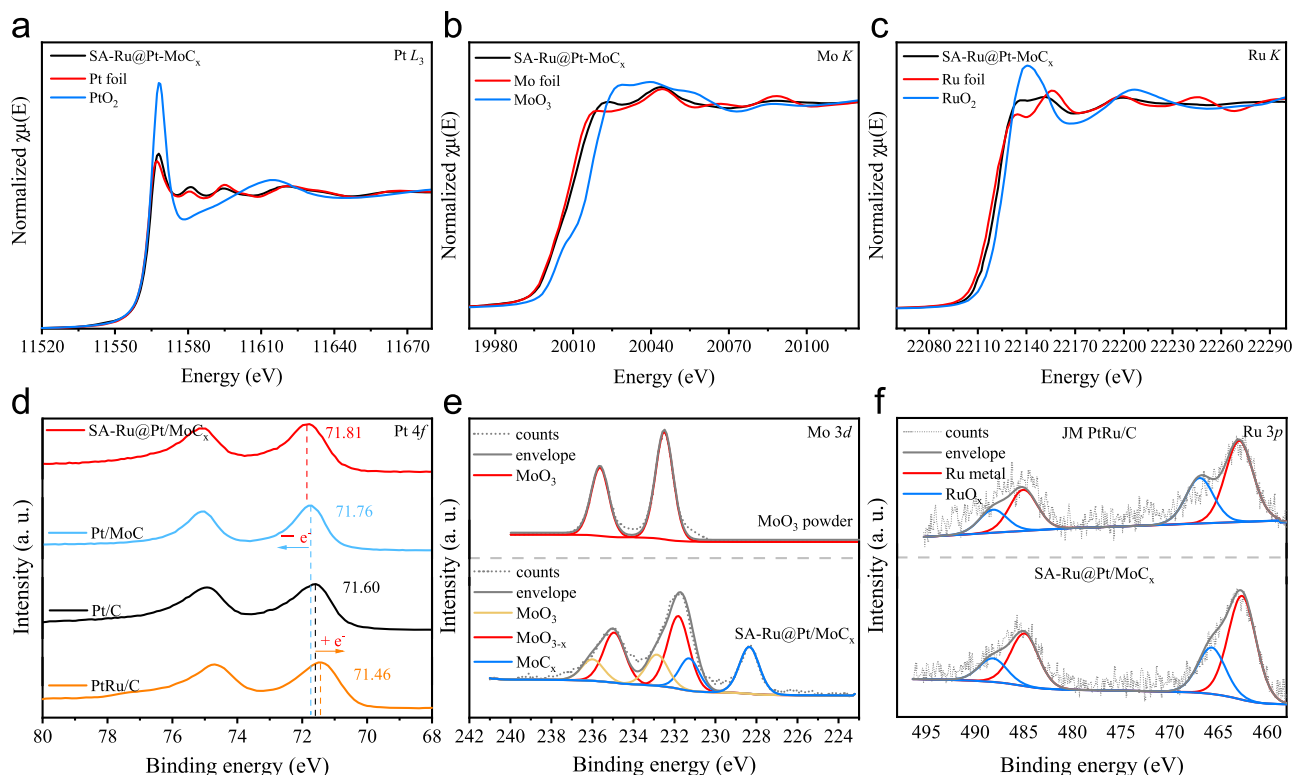


**Fig. 4 | Electronic structure characterizations.** **a** Pt  $L_3$ -edge XANES spectra of SA-Ru@Pt/MoC<sub>x</sub>, PtO<sub>2</sub> and Pt foil. **b** Mo K-edge XANES spectra of SA-Ru@Pt/MoC<sub>x</sub>, MoO<sub>3</sub> and Mo foil. **c** Ru K-edge XANES spectra of SA-Ru@Pt/MoC<sub>x</sub>, RuO<sub>2</sub> and Ru foil. **d–f** The XPS spectra of Pt 4f, Mo 3d and Ru 3p in SA-Ru@Pt/MoC<sub>x</sub> and reference samples.

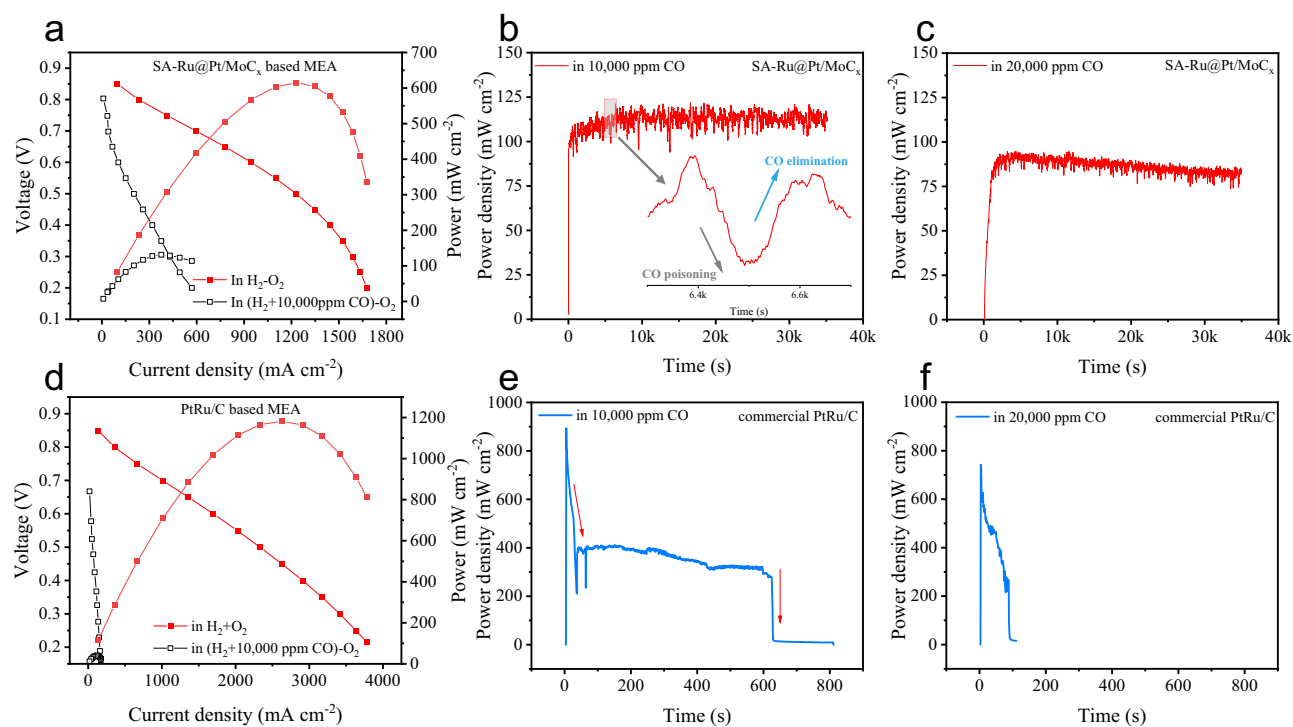


**Fig. 5 | Activity and CO tolerance tests in PEMFC.** **a, d** The PEMFC performance of SA-Ru@Pt/MoC<sub>x</sub> and commercial PtRu based MEA in H<sub>2</sub>-O<sub>2</sub> and H<sub>2</sub> + 10,000 ppm CO-O<sub>2</sub> environment. The Pt loading is 0.1 mg cm<sup>-2</sup>. All the gas is 100% relative humidity (RH) and the cell temperature was set at 80 °C with 200 kPa back pressure. **b, c, e, f** The power-time curves for SA-Ru@Pt/MoC<sub>x</sub> and commercial PtRu based MEA with H<sub>2</sub> + 10,000 ppm CO and H<sub>2</sub> + 20,000 ppm CO as anode gas respectively.

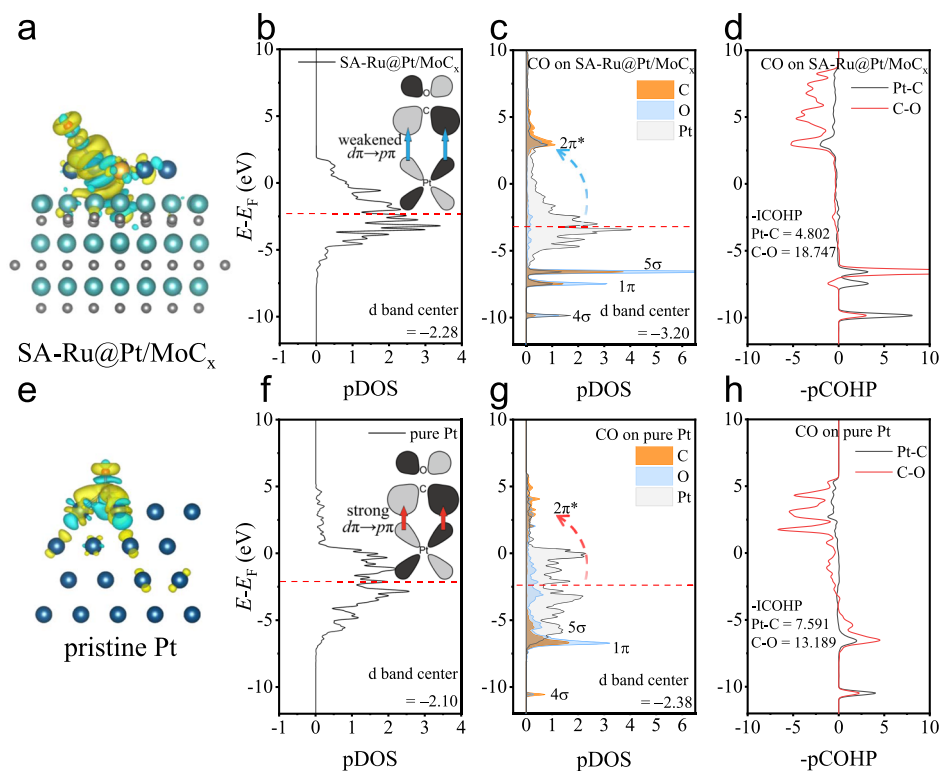


**Fig. 6 | DFT studies of the electronic structure and bonding character.** **a** The charge-density difference (CDD) of SA-Ru@Pt/MoC<sub>x</sub> with an adsorbed CO molecule. **b** pDOS of Pt in SA-Ru@Pt/MoC<sub>x</sub> before CO adsorption. **c** pDOS of Pt and CO when CO had adsorbed on SA-Ru@Pt/MoC<sub>x</sub>, and corresponding -pCOHP of Pt-C

and C-O bonds (**d**). **e** The CDD of Pt with an adsorbed CO molecule. **f** pDOS of pristine Pt before CO adsorption. **g** pDOS of Pt and CO when CO was adsorbed, and corresponding -pCOHP of Pt-C and C-O bonds (**h**).

potential scans (0.2–0.8 V). Unexpectedly, after the same potential loop test, the power of the SA-Ru@Pt/MoC<sub>x</sub>-based MEA remained 21.4% of the maximum power in pure H<sub>2</sub> and stabilized at 131 mW cm<sup>-2</sup>.

Then, to test the long-term stability in CO-containing environment, the constant voltage experiment was conducted at 0.45 V, which is the condition for maximum output power. As shown in Fig. 5e, commercial PtRu/C exhibited a dramatic drop in power density at the beginning of pumping 10,000 ppm CO/H<sub>2</sub> mixture into the anode and was completely poisoned after running for 620 s. In a sharp contrast, SA-Ru@Pt/MoC<sub>x</sub> exhibited a steady output power of about 110 mW cm<sup>-2</sup> for 35,000 s (Fig. 5b). When the CO concentration was further improved to 20,000 ppm, the commercial PtRu-based MEA shut down completely within 100 s (Fig. 5f). While the SA-Ru@Pt/MoC<sub>x</sub> based MEA can still operate with an average output power of 88 mW cm<sup>-2</sup> in 35,000 s (gradually decreased by 10.2%) (Fig. 5c). The power density oscillation during the stability test can be clearly seen in the inset of Fig. 5b. The decrease of power density is attributed to the poisoning of Pt sites by CO adsorption, and the increase is attributed to the regeneration of Pt sites after CO elimination. The alternative occurrence of these two processes is the typical feature of the regeneration of poisoned Pt sites, which reserves Pt sites for continually continuously catalyzing HOR<sup>53–55</sup>. Although PtRu/C-based MEA exhibited a certain degree of power density oscillation, the poor CO removal ability of PtRu/C leads to the persistent poisoning of the Pt active site by CO and eventually lost all of its HOR activity.

To figure out the real high CO tolerant sites of SA-Ru@Pt/MoC<sub>x</sub>, we conducted several comparative experiments by improving the Pt loading and adding carbon powder (Vulcan XC-72). As shown in Supplementary Fig. 16a, The SA-Ru@Pt/MoC<sub>x</sub>-0.4 based MEA with higher Pt loading (0.4 mg<sub>Pt</sub> cm<sup>-2</sup>) also shows an inferior initial power (655 mW cm<sup>-2</sup>) in H<sub>2</sub>-O<sub>2</sub> mode also compared to the commercial catalyst. While, SA-Ru@Pt/MoC<sub>x</sub>-MEA-0.4 exhibited a doubled output power

density in H<sub>2</sub> + 20,000 ppm CO atmosphere (182 mW cm<sup>-2</sup> vs. SA-Ru@Pt/MoC<sub>x</sub>, 88 mW cm<sup>-2</sup>) and was still able to operate stably (Supplementary Fig. 16b). This result suggests that most of the additional Pt added was not used to enhance activity, but some of the Pt formed new sites with high resistance to CO. The majority of the Pt may be embedded in the sintered metal blocks (Supplementary Fig. 7). We further added carbon powder with high specific surface area (vulcan XC-72) during the process of synthesis to prepare sample C-SA-Ru@Pt/MoC<sub>x</sub> for increasing the electrical conductivity and metal dispersity. The initial output power of C-SA-Ru@Pt/MoC<sub>x</sub> was significantly improved (Pt loading = 0.1 mg<sub>Pt</sub> cm<sup>-2</sup>, 1460 mW cm<sup>-2</sup> Supplementary Fig. 17a) and the electrochemical impedance spectroscopy (EIS) of C-SA-Ru@Pt/MoC<sub>x</sub> was reduced as compared with SA-Ru@Pt/MoC<sub>x</sub> (Supplementary Fig. 20). While the output power (174 mW cm<sup>-2</sup>) in H<sub>2</sub> + 10,000 ppm CO was not doubled (vs. SA-Ru@Pt/MoC<sub>x</sub>, 110 mW cm<sup>-2</sup>) (Supplementary Fig. 17b). Moreover, to exclude the influence of alloy blocks, the PtMo/C-based MEA was also prepared and tested in H<sub>2</sub> + 10,000 ppm CO environment, which failed to operate sustainably, indicating that the large amorphous PtMo particles do not contribute to the CO tolerance of SA-Ru@Pt/MoC<sub>x</sub> (Supplementary Fig. 18). These experiments demonstrate that the highly CO-resistant reactive sites are not derived from simple PtRu or PtMo alloys. Considering that sites with special properties often originate from the fine surface structure of the catalyst rather than from the bulk, we further investigated the chemical properties of the most probable Pt-MoC<sub>x</sub>-SA-Ru structure for high CO tolerance capability using theoretical calculations.

#### DFT investigation on the CO tolerant mechanism

To understand why the electron-deficient Pt in SA-Ru@Pt/MoC<sub>x</sub> exhibits high CO tolerance, density functional theory (DFT) calculations were performed based on the experimentally determined structure. By comparing Fig. 6b, f, it can be found that when MoC<sub>x</sub>

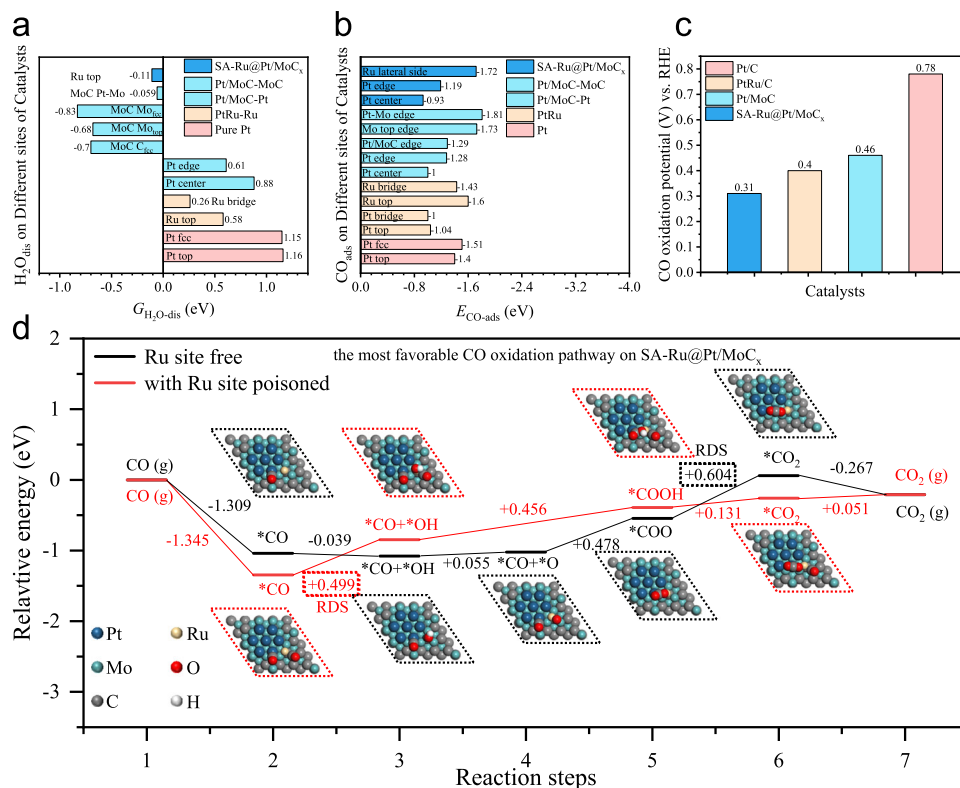


**Fig. 7 | DFT calculations for the adsorption and reaction behavior of different catalyst surfaces. a, b** The water dissociation energy and CO adsorption energy of different sites on SA-Ru@Pt/MoC<sub>x</sub> and reference samples. **c** The experimental

onset potential of CO oxidation on different samples. **d** Energy profiles of CO oxidation on SA-Ru@Pt/MoC<sub>x</sub> (with or without Ru poisoned).

was used as the support for Pt, the d-band center of Pt shifted downward, making it electron-deficient and thus weakening the electron backdonation to CO<sub>ads</sub> (Fig. 6b, f and Supplementary Fig. 21)<sup>31,56,57</sup>. Figure 6c, g shows the density of states (DOS) of Pt when CO is adsorbed. It can be seen that the d-band center of Pt appears to be further downshifted and the d-band center of Pt in SA-Ru@Pt/MoC<sub>x</sub> is more far away from the antibonding orbital of CO compared to the case of pure Pt. And the molecular orbitals of the CO<sub>ads</sub> (1π and 5σ) on SA-Ru@Pt/MoC<sub>x</sub> overlap less with the d-band of Pt in the -5 - -7.5 eV range, while the molecular orbitals of CO<sub>ads</sub> on pure Pt overlap more with the Pt d-band in this energy range. We further investigated the bonding strength of Pt to CO<sub>ads</sub> and the C-O bond strength within CO using the projected crystal orbital Hamilton population (-pCOHP) (Fig. 6d, h). It can be seen that the integrated COHP (-ICOHP) of Pt-C bond on SA-Ru@Pt/MoC<sub>x</sub> (4.802) is significantly smaller than that on pure Pt (7.591), indicating weaker adsorption of CO<sub>ads</sub> on SA-Ru@Pt/MoC<sub>x</sub><sup>58,59</sup>. And the internal C-O bond strength of CO<sub>ads</sub> on SA-Ru@Pt/MoC<sub>x</sub> (-ICOHP = 18.747) is stronger than that of pure Pt (-ICOHP = 13.189), which also indicates the weaker CO adsorption by the reduction of the electron backdonation from SA-Ru@Pt/MoC<sub>x</sub> to CO<sub>ads</sub>.

We further calculated the adsorption energy to CO ( $E_{\text{CO-ads}}$ ) and the free energy of water dissociation ( $G_{\text{H}_2\text{O-dis}}$ ) at different sites for different catalysts (Fig. 7a, b and Supplementary Tables 2 and 3). It can be found that the  $E_{\text{CO-ads}}$  on Pt was decreased after modulation by MoC, and it was further reduced by the addition of SA-Ru. These results are consistent with the half-cell CO stripping results (Fig. 7c and Supplementary Fig. 12). It is noted that the CO oxidation potential of PtRu/C is lower than that of Pt/MoC<sub>x</sub> in the half-cell test, whereas in the full-cell, PtRu/C-based MEA fails to operate stably. In fact, the calculation result shows that the Ru sites in PtRu alloys are also susceptible to CO poisoning (Supplementary Fig. 23 and Table 2), which is in

agreement with previous results reported in the literature<sup>33-37</sup>. This suggests that a good CO-tolerant catalysts requires CO-immune sites to continuously supply -OH for CO oxidation. According to the calculation results, only the SA-Ru and MoC<sub>x</sub> surface sites in SA-Ru@Pt/MoC<sub>x</sub> are capable of spontaneously dissociating water. The MoC<sub>x</sub> surface can be hydroxylated very easily and the \*O on its surface will assist in the removal of CO<sub>ads</sub> on edge-of Pt and CO within the gas stream (Supplementary Fig. 24). Moreover, even when a CO molecule is already adsorbed on SA-Ru, it still acts as a stable water dissociation site and produces -OH to help CO<sub>ads</sub> oxidation on Pt (Fig. 7d and Supplementary Fig. 29). This explains the ability of the reference sample, Pt/MoC<sub>x</sub>, to operate stably in CO-containing environments and the better performance of SA-Ru@Pt/MoC<sub>x</sub> when Ru-SA was added (Supplementary Fig. 19). Meanwhile, the detailed reaction pathway profiles show that CO<sub>ads</sub> oxidation by -OH generated on SA-Ru has the lowest reaction energy barrier compared to other reference samples, which further gives the reason for the high CO-tolerant performance of SA-Ru@Pt/MoC<sub>x</sub> in the full-cell test (Supplementary Figs. 25-28).

In summary, we have constructed a highly CO-tolerant Pt-based HOR catalyst that consisting of Pt clusters (2 nm) supported on MoC<sub>x</sub> substrate surrounded by a large amount of SA-Ru. The MoC<sub>x</sub> support modulates the electronic structure of Pt and weakens the CO adsorption strength. More importantly, the Mo sites on MoC<sub>x</sub> serve as H<sub>2</sub>O dissociation sites to provide surface \*O for the oxidation of CO<sub>ads</sub> on neighboring Pt and CO (g) in the fuel. In addition, the SA-Ru next to the Pt cluster can act as a CO-immune site that continuously produces -OH to help CO<sub>ads</sub> oxidation and help regenerate the active site of Pt. These properties make the SA-Ru catalyst superior to other catalysts in terms of CO resistance. Even though the current synthesis method yields some undesired metal blocks in the product. We believe that this electronic modulation combined with surface fine structure



construction strategy will provide a reference for the future synthesis of CO-resistant catalysts as well as some catalysts with special selectivity.

## Methods

### chemicals and materials

Commercial Pt/C (Johnson Matthey) and PtRu/C (Sigma-Aldrich, TANAKA), ammonium molybdate (Chongqing Chuandong Chemical Co., Ltd.), tetraammineplatinum chloride (Shanghai Jiuyue Chemical Engineering Co., Ltd.), ruthenium trichloride (Shanghai Aladdin Biochemical Technology Co., Ltd), dopamine hydrochloride (Sigma-Aldrich), tris(hydroxymethyl)aminomethane (MERDA technology Co., Ltd. USA), tetraethyl orthosilicate (TEOS), ethylene glycol and hydrofluoric acid (Chengdu Kelong Chemical Reagent Factory), hydrochloric acid and nitric acid (Chongqing Chuandong Chemical Co., Ltd.), deionized water (purification system from Chongqing Huachuang Water Treatment Engineering Co., Ltd.), and N<sub>2</sub>, O<sub>2</sub>, H<sub>2</sub>, (H<sub>2</sub>+10,000 ppm CO), (H<sub>2</sub>+20,000 ppm CO) (national standard reference authenticated) from Chongqing Ruixin Gas Co., Ltd.

All chemical reagents were guarantee reagent and used as received without the further purification.

### Preparation of MoO<sub>3</sub> precursor

The precursor MoO<sub>3</sub> nanorod was synthesized by a hydrothermal method. In a typical process, 1.4 g (NH<sub>4</sub>)<sub>6</sub>Mo<sub>7</sub>O<sub>24</sub>·4H<sub>2</sub>O was added to a 40 mL mixture of deionized H<sub>2</sub>O and HNO<sub>3</sub> (5:1 in volume) and underwent 200 °C, 12 h hydrothermal process. The obtained solid (MoO<sub>3</sub>) in PTFE filter reactor was collected by vacuum filtration.

### Preparation of SA-Ru@Pt/MoC<sub>x</sub>

One mL of tetraammineplatinum chloride monohydrate ((NH<sub>3</sub>)<sub>4</sub>PtCl<sub>2</sub>) solution (0.24 mM) and 200 mg MoO<sub>3</sub> were mixed in a round-bottom flask, then 20 mL ethylene glycol was added to the bottle. The mixture was subsequently reduced by ethylene glycol under 180 °C. The obtained 200 mg of Pt/MoO<sub>3</sub> was dispersed in 25 of mL Tris-HCl water solution (pH=9) and 50 mg of dopamine was added and stirred for 12 h. Then 2 mL RuCl<sub>3</sub> solution (0.12 mM) was added to the beaker for another 12 h. After that, 3 mL HCl (pH=1) and 3 mL TEOS were added to the beaker. After 6 h hydrolysis, the sample was collected by vacuum filtration. The as obtained sample was denoted as SiO<sub>2</sub>@PDA-Ru<sup>3+</sup>@Pt/MoO<sub>3</sub> according to its component from outside to inside. Subsequently the samples were heated up to 700 °C in a tube furnace at 5 °C per minute and annealed for 2 h in an atmosphere of H<sub>2</sub>+N<sub>2</sub> (1:9). Finally, the SiO<sub>2</sub> shell was etched with HF solution (20%) for 4 h to obtain SA-Ru@Pt/MoC<sub>x</sub>.

### Material characterization

The transmission electron microscopy (TEM) was conducted on field emission transmission electron microscope (Thermo Fisher Scientific Talos F200S) operated at an acceleration voltage of 200 kV. High-resolution transmission electron microscopy (HRTEM) and high angle annular dark field (HAADF) observations were carried out on spherical aberration corrector transmission electron microscopy (FEI Thaims Z, Titan Cubed Themis G2300, JEM-ARM200F). The XPS measurements were conducted on a ESCALAB250Xi spectrometer using a monochromated Al K $\alpha$  radiation (hv=1486.6 eV). X-ray diffraction (XRD) data were collected on a X-ray diffractometer (Empyrean Alpha 1, Malvern Panalytical Co., Ltd. Netherlands) at a scanning rate of 5° min<sup>-1</sup>. The inductively coupled plasma (ICP) measurements were conducted on 5110 (OES) (Agilent). The X-ray absorption fine structure spectra of SA-Ru@Pt/MoC<sub>x</sub> and reference samples were collected at 1W1B station in Beijing Synchrotron Radiation Facility (BSRF) (Beijing, China). Raw data of Pt, Ru and Mo were processed using Athena and Artemis software under *k*<sup>3</sup>-weighted conditions<sup>60</sup>. The wavelet transform analysis was processed using HAMA FORTRAN software<sup>61,62</sup>.

### Electrochemical measurements

**Equipment preparation.** The electrochemical test was carried on electrochemical workstation (VersaSTAT 3F, Princeton Applied Research) assisted by rotating ring disc electrode (RRDE, PINE: AFE3T050GC). The test was conducted in a three electrodes system. Glass carbon disk electrode was used as working electrode (WE). Graphite rod was used as the counter electrode (CE). Ag/AgCl (3 M KCl) electrode was used as reference electrode (RE) and calibrated in H<sub>2</sub> saturated 0.1 M HClO<sub>4</sub> solution with Pt coil as WE and CE.

**Preparation of catalyst ink and working electrode.** Two mg catalyst (40% Pt wt.%), 800  $\mu$ L ethanol and 10  $\mu$ L 5 wt.% Nafion (Dupont) were added to a centrifuge tube and then conducted by ultrasonic processing for 20 min. Five  $\mu$ L of ink was pipetted by pipettor to the surface of glass carbon and then dried under infrared lamp. The reference sample electrode of Pt/C (Johnson Matthey In. UK) and PtRu/C (Sigma-Aldrich) were prepared by same procedure. And the loading of Pt is 25  $\mu$ g cm<sup>-2</sup> respectively.

**Testing methods.** Activation: the working electrode covered with catalysts was activated by 50 cycles of cyclic voltammetry (CV) in N<sub>2</sub>-saturated 0.1 M HClO<sub>4</sub> at a scan rate of 50 mV/s.

Characterization of hydrogen oxidation reaction (HOR) activity: the WE was subjected to liner scanning voltammetry in H<sub>2</sub>-saturated 0.1 M HClO<sub>4</sub> at a scan rate of 5 mV/s from -0.05 V to 0.5 V (vs. RHE) and the rotation speed of WE was set at 1600 rpm.

Characterization of anti-CO ability: the method is the same as testing of HOR, but the solution is saturated by H<sub>2</sub> contains 20,000 ppm CO.

Constant potential measurement for HOR and anti-CO ability: 0.1 V potential (vs. RHE) was applied on the WE for chronoamperometry (CA) in pure H<sub>2</sub>-saturated 0.1 M HClO<sub>4</sub> and H<sub>2</sub>+20,000 ppm CO saturated 0.1 M HClO<sub>4</sub> respectively.

Test of CO stripping curve: the WE was first immersed in CO saturated 0.1 M HClO<sub>4</sub> and chronoamperometry was performed for 10 min at 0.1 V (vs. RHE) for absolute adsorption CO. And the CO-stripping curve was obtained by CV scan at 10 mV/s in N<sub>2</sub>-saturated 0.1 M HClO<sub>4</sub>.

### MEA preparation and fuel cell measurement

**Ink preparing.** A certain amount of SA-Ru@Pt/MoC<sub>x</sub> and reference samples were weighed to make sure the loading of Pt is 0.1 mg cm<sup>-2</sup>. The catalysts and 10  $\mu$ L 5 wt.% Nafion (Dupont) were ultrasonically mixed with 0.8 mL isopropyl for 15 min respectively. The ink of Pt/C for cathode was prepared with the same method and the Pt loading is 0.1 mg cm<sup>-2</sup>.

**MEA preparing.** The cathode and anode inks were sprayed on each side of the Nafion membrane (Nafion HP) with an airbrush. After that, the membrane is sandwiched between two pieces of carbon paper (HCP-120) and heat-pressed at 135 °C. The MEA was pressed under 350 psi for 10 s and then increase the pressure to 700 psi for 150 s.

**Single cell testing.** The MEA was loaded on fuel cell test system (Model 850e Scribner Associates Incorporated). The pure hydrogen and oxygen were used in the anode (250 mL min<sup>-1</sup>) and cathode (350 mL min<sup>-1</sup>). All the gas is 100% relative humidity (RH) and the cell temperature was set at 80 °C with 200 kPa back pressure.

The repeat loop scanning was set between 0.2 V and 0.9 V for 30 cycles until the output power getting stable. Then anti-CO testing was conducted by switch the anode gas to H<sub>2</sub> with CO.

The constant voltage test of the catalysts was performed at 0.45 V, which is the condition for maximum output power.



## DFT calculations

All DFT calculation were carried out by using the Perdew-Burke-Ernzerhof (PBE) functional in the Vienna ab initio simulation package (VASP). The exchange correlation was performed within generalized gradient approximation (GGA). The cutoff kinetic energy was set as 450 eV. The convergence criterion of energy and force were set to  $10^{-5}$  eV/atom and 0.02 eV/Å. The  $2 \times 2 \times 1$  (Gamma sample method) and  $3 \times 3 \times 1$  (Monkhorst-Pack sample method) k-point grid were used in MoC-based model and alloy model respectively with 15 Å vacuum distance to keep in equal precision. And the DFT-D3 was adopted to provide dispersion correction in van der Waals (vdW) interaction. The Gibbs free energy is determined following  $\Delta G = \Delta E + \Delta E_{ZPE} + T\Delta S$ , where  $\Delta E$ ,  $\Delta E_{ZPE}$ ,  $\Delta S$  are the electronic total energy differences, the differences in the zero point energy and the change of entropy, respectively.  $T$  is the temperature set as 298.15 K. We added an implicit solvation effect (vaspsol) on the system to our calculations, where the dielectric constant of water is 78.4 (EB\_k = 78.4).

## Reporting summary

Further information on research design is available in the Nature Portfolio Reporting Summary linked to this article.

## Data availability

All relevant data generated in this study are provided in the Supplementary Information/Source Data file.

## References

- Ke, S., Sun, C., Cui, B., Qin, Y. & Dou, M. Operable and efficient mitigation strategies for H<sub>2</sub>S poisoning in proton exchange membrane fuel cells: releasing Pt reactive sites for hydrogen oxidation. *ACS Appl. Energy Mater.* **6**, 3337–3346 (2023).
- Li, Z. et al. Recent advances in the anode catalyst layer for proton exchange membrane fuel cells. *Renew. Sustain. Energy Rev.* **176**, 113182 (2023).
- Yang, X. et al. CO-tolerant PEMFC anodes enabled by synergistic catalysis between iridium single-atom sites and nanoparticles. *Angew. Chem. Int. Ed. Engl.* **60**, 26177–26183 (2021).
- Li, Y. et al. Carbon monoxide powered fuel cell towards H<sub>2</sub>-onboard purification. *Sci. Bull.* **66**, 1305–1311 (2021).
- Pan, H. R. et al. CO-tolerant hydrogen oxidation electrocatalysts for low-temperature hydrogen fuel cells. *J. Phys. Chem. Lett.* **15**, 3011–3022 (2024).
- Wang, T. et al. High CO-tolerant Ru-based catalysts by constructing an oxide blocking layer. *J. Am. Chem. Soc.* **144**, 9292–9301 (2022).
- Tang, M. et al. Single-atom catalysts for proton exchange membrane fuel cell: anode anti-poisoning & characterization technology. *Electrochim. Acta* **446**, 142120 (2023).
- Pei, P., Wang, M., Chen, D., Ren, P. & Zhang, L. Key technologies for polymer electrolyte membrane fuel cell systems fueled impure hydrogen. *Prog. Nat. Sci. Mater. Int.* **30**, 751–763 (2020).
- Wang, X. et al. Proton exchange membrane fuel cells powered with both CO and H<sub>2</sub>. *Proc. Natl Acad. Sci. USA* **118**, e2107332118 (2021).
- Zhou, Y. et al. Lattice-confined Ru clusters with high CO tolerance and activity for the hydrogen oxidation reaction. *Nat. Catal.* **3**, 454–462 (2020).
- Tang, T. et al. Unconventional bilateral compressive strained Ni-Ir interface synergistically accelerates alkaline hydrogen oxidation. *J. Am. Chem. Soc.* **145**, 13805–13815 (2023).
- Yu, W., Porosoff, M. D. & Chen, J. G. Review of Pt-based bimetallic catalysis: from model surfaces to supported catalysts. *Chem. Rev.* **112**, 5780–5817 (2012).
- Wang, Q. et al. Surface Ru enriched structurally ordered inter-metallic PtFe@PtRuFe core-shell nanostructure boosts methanol oxidation reaction catalysis. *Appl. Catal. B Environ.* **252**, 120–127 (2019).
- Gasteiger, H. A., Markovic, N., Ross, P. N. & Cairns, E. J. Carbon monoxide electrooxidation on well-characterized platinum-ruthenium alloys. *J. Phys. Chem.* **98**, 617–625 (1994).
- Watanabe, M. & Motoo, S. Electrocatalysis by ad-atoms. *J. Electroanal. Chem. Interfacial Electrochem.* **60**, 275–283 (1975).
- Yang, L. et al. Stabilizing Pt electrocatalysts via introducing reducible oxide support as reservoir of electrons and oxygen species. *ACS Catal.* **12**, 13523–13532 (2022).
- Chen, W. et al. Molecular-level insights into the notorious CO poisoning of platinum catalyst. *Angew. Chem. Int. Ed. Engl.* **61**, e202200190 (2022).
- Blyholder, G. Molecular orbital view of chemisorbed carbon monoxide. *J. Phys. Chem.* **68**, 2772–2777 (1964).
- Molochas, C. & Tsiakaras, P. Carbon monoxide tolerant Pt-based electrocatalysts for H<sub>2</sub>-PEMFC applications: current progress and challenges. *Catalysts* **11**, 1127 (2021).
- Igarashi, H., Fujino, T., Zhu, Y., Uchida, H. & Watanabe, M. CO tolerance of Pt alloy electrocatalysts for polymer electrolyte fuel cells and the detoxification mechanism. *Phys. Chem. Chem. Phys.* **3**, 306–314 (2001).
- Yang, Y. et al. Suppressing electron back-donation for a highly CO-tolerant fuel cell anode catalyst via cobalt modulation. *Angew. Chem. Int. Ed. Engl.* **61**, e202208040 (2022).
- Yang, Z. et al. Tailoring interfacial chemistry of defective carbon-supported Ru catalyst toward efficient and CO-tolerant alkaline hydrogen oxidation reaction. *Adv. Energy Mater.* **13**, 2300881 (2023).
- Dong, Z. et al. Synergistically mitigating electron back-donation by single-atomic Fe–N–C and alloying to boost CO-tolerance of Pt in hydrogen oxidation. *ACS Catal.* **13**, 7822–7830 (2023).
- Yang, Y. et al. Unleashing efficient and CO-resilient alkaline hydrogen oxidation of Pd<sub>3</sub>P through phosphorus vacancy defect engineering. *Chin. J. Catal.* **56**, 176–187 (2024).
- Hunt, S. T. et al. Self-assembly of noble metal monolayers on transition metal carbide nanoparticle catalysts. *Science* **352**, 974–978 (2016).
- Luo, H. et al. Amorphous MoO<sub>x</sub> with high oxophilicity interfaced with PtMo alloy nanoparticles boosts anti-CO hydrogen electrocatalysis. *Adv. Mater.* **35**, 2211854 (2023).
- Shi, G., Yano, H., Tryk, D. A., Iiyama, A. & Uchida, H. Highly active, CO-tolerant, and robust hydrogen anode catalysts: Pt–M (M = Fe, Co, Ni) alloys with stabilized Pt-skin layers. *ACS Catal.* **7**, 267–274 (2016).
- Wang, S. et al. Local oxidation induced amorphization of 1.5-nm-thick Pt–Ru nanowires enables superactive and CO-tolerant hydrogen oxidation in alkaline media. *Adv. Funct. Mater.* **33**, 2304125 (2023).
- Yang, C. et al. Metal alloys-structured electrocatalysts: metal-metal interactions, coordination microenvironments, and structural property-reactivity relationships. *Adv. Mater.* **35**, e2301836 (2023).
- Wang, X. et al. Atomic-precision Pt<sub>6</sub> nanoclusters for enhanced hydrogen electro-oxidation. *Nat. Commun.* **13**, 1596 (2022).
- Yang, Z. et al. Pt single atoms on CrN nanoparticles deliver outstanding activity and CO tolerance in the hydrogen oxidation reaction. *Adv. Mater.* **35**, 2208799 (2022).
- Koper, M. T. M., Shubina, T. E. & van Santen, R. A. Periodic density functional study of CO and OH adsorption on Pt–Ru alloy surfaces: implications for CO tolerant fuel cell catalysts. *J. Phys. Chem. B* **106**, 686–692 (2001).
- Baz, A. & Holecinski, A. Understanding the interplay of bifunctional and electronic effects: microkinetic modeling of the CO electro-oxidation reaction. *J. Catal.* **384**, 1–13 (2020).
- Zhao, L. et al. The oxidation of methanol on PtRu(111): a periodic density functional theory investigation. *J. Phys. Chem. C* **119**, 20389–20400 (2015).

35. Ding, Q. et al. Insight into the reaction mechanisms of methanol on PtRu/Pt(111): a density functional study. *Appl. Surf. Sci.* **369**, 257–266 (2016).
36. Liu, P., Logadottir, A. & Nørskov, J. K. Modeling the electro-oxidation of CO and H<sub>2</sub>/CO on Pt, Ru, PtRu and Pt<sub>3</sub>Sn. *Electrochim. Acta* **48**, 3731–3742 (2003).
37. Ge, Q., Desai, S., Neurock, M. & Kourtakis, K. CO adsorption on Pt–Ru surface alloys and on the surface of Pt–Ru bulk alloy. *J. Phys. Chem. B* **105**, 9533–9536 (2001).
38. Dong, J., Fu, Q., Jiang, Z., Mei, B. & Bao, X. Carbide-supported Au catalysts for water-gas shift reactions: a new territory for the strong metal-support interaction effect. *J. Am. Chem. Soc.* **140**, 13808–13816 (2018).
39. Wei, S. et al. Direct observation of noble metal nanoparticles transforming to thermally stable single atoms. *Nat. Nanotechnol.* **13**, 856–861 (2018).
40. Zhang, X. et al. A stable low-temperature H<sub>2</sub>-production catalyst by crowding Pt on alpha-MoC. *Nature* **589**, 396–401 (2021).
41. Mao, J. et al. Design of ultrathin Pt–Mo–Ni nanowire catalysts for ethanol electrooxidation. *Sci. Adv.* **3**, e1603068 (2017).
42. Liu, S. et al. Vacancy-coordinated hydrogen evolution reaction on MoO<sub>3</sub>-x anchored atomically dispersed MoRu pairs. *J. Mater. Chem. A* **7**, 14466–14472 (2019).
43. Wang, Z. et al. Single Ru atoms with precise coordination on a monolayer layered double hydroxide for efficient electrooxidation catalysis. *Chem. Sci.* **10**, 378–384 (2019).
44. Zhang, L. et al. Atomic layer deposited Pt–Ru dual-metal dimers and identifying their active sites for hydrogen evolution reaction. *Nat. Commun.* **10**, 4936 (2019).
45. Li, C. et al. P and Mo dual doped Ru ultrasmall nanoclusters embedded in P-doped porous carbon toward efficient hydrogen evolution reaction. *Adv. Energy Mater.* **12**, 2200029 (2022).
46. Zhang, E. et al. Electron localization in rationally designed Pt(1)Pd single-atom alloy catalyst enables high-performance Li–O(2) batteries. *J. Am. Chem. Soc.* **146**, 2339–2344 (2024).
47. Xu, M. et al. Kinetically matched C–N coupling toward efficient urea electrosynthesis enabled on copper single-atom alloy. *Nat. Commun.* **14**, 6994 (2023).
48. Deng, Y. et al. Molybdenum carbide: controlling the geometric and electronic structure of noble metals for the activation of O–H and C–H bonds. *Acc. Chem. Res.* **52**, 3372–3383 (2019).
49. Lin, L. et al. Low-temperature hydrogen production from water and methanol using Pt/alpha-MoC catalysts. *Nature* **544**, 80–83 (2017).
50. Matin, M. A., Lee, E., Kim, H., Yoon, W.-S. & Kwon, Y.-U. Rational syntheses of core–shell Fe@(PtRu) nanoparticle electrocatalysts for the methanol oxidation reaction with complete suppression of CO-poisoning and highly enhanced activity. *J. Mater. Chem. A* **3**, 17154–17164 (2015).
51. Ge, R. et al. Selective electrooxidation of biomass-derived alcohols to aldehydes in a neutral medium: promoted water dissociation over a nickel-oxide-supported ruthenium single-atom catalyst. *Angew. Chem. Int. Ed.* **61**, e202200211 (2022).
52. Wang, Q., Wang, G., Tao, H., Li, Z. & Han, L. Highly CO tolerant PtRu/PtNi/C catalyst for polymer electrolyte membrane fuel cell. *RSC Adv.* **7**, 8453–8459 (2017).
53. Kadyk, T., Kirsch, S., Hanke-Rauschenbach, R. & Sundmacher, K. Autonomous potential oscillations at the Pt anode of a polymer electrolyte membrane fuel cell under CO poisoning. *Electrochim. Acta* **56**, 10593–10602 (2011).
54. Zhang, J., Fehribach, J. D. & Datta, R. Mechanistic and bifurcation analysis of anode potential oscillations in PEMFCs with CO in anode feed. *J. Electrochem. Soc.* **151**, A689–A697 (2004).
55. Lopes, P. P., Ticianelli, E. A. & Varela, H. Potential oscillations in a proton exchange membrane fuel cell with a Pd–Pt/C anode. *J. Power Sources* **196**, 84–89 (2011).
56. Zhang, J. et al. Engineering the near-surface of PtRu<sub>3</sub> nanoparticles to improve hydrogen oxidation activity in alkaline electrolyte. *Small* **17**, 2006698 (2021).
57. Freitas, K. S., Lopes, P. P. & Ticianelli, E. A. Electrocatalysis of the hydrogen oxidation in the presence of CO on RhO<sub>2</sub>/C-supported Pt nanoparticles. *Electrochim. Acta* **56**, 418–426 (2010).
58. Lin, L. et al. A highly CO-tolerant atomically dispersed Pt catalyst for chemoselective hydrogenation. *Nat. Nanotechnol.* **14**, 354–361 (2019).
59. Foppa, L., Coperet, C. & Comas-Vives, A. Increased back-bonding explains step-edge reactivity and particle size effect for CO activation on Ru nanoparticles. *J. Am. Chem. Soc.* **138**, 16655–16668 (2016).
60. Ravel, B. & Newville, M. ATHENA, ARTEMIS, HEPHAESTUS: data analysis for X-ray absorption spectroscopy using IFEFFIT. *J. Synchrotron Radiat.* **12**, 537–541 (2005).
61. Funke, H., Scheinost, A. C. & Chukalina, M. Wavelet analysis of extended x-ray absorption fine structure data. *Phys. Rev. B* **71**, 094110 (2005).
62. Funke, H., Chukalina, M. & Scheinost, A. C. A newFEFF-based wavelet for EXAFS data analysis. *J. Synchrotron Radiat.* **14**, 426–432 (2007).

## Acknowledgements

This study was financially supported by the National Key R&D Program of China (2020YFB1506002, S.C.), the National Natural Science Foundation of China (grant nos. 22178034 and 21978028, S.C.; grant no. 22108020, M.W.) and the Chongqing Talent Program (cstc2022ycjh-bgzxm0096, S.C.). The numerical calculations in this paper have been done on Hefei advanced computing center. The authors extend their gratitude to Shiyanjia Lab ([www.shiyanjia.com](http://www.shiyanjia.com)) for providing XPS and AC-HAADF-STEM experimental instruments.

## Author contributions

S.C., Z.W. and D.L. conceived the project. S.C. directed the main experimental works. S.C., D.L., X.T. and X.P. analyzed the experimental data. D.L. carried out the sample synthesis, characterization, electrochemical measurements. Y.L. carried out DFT calculation. L.L. provided suggestions for theoretical calculations. F.C. and M.W. participated in some of the experimental work. Z.X. performed the electron-microscopy characterization. D.L., S.C., L.G. and Z.W. wrote the manuscript together.

## Competing interests

The authors declare no competing interests.

## Additional information

**Supplementary information** The online version contains supplementary material available at <https://doi.org/10.1038/s41467-024-51562-9>.

**Correspondence** and requests for materials should be addressed to Lin Guo or Siguo Chen.

**Peer review information** *Nature Communications* thanks Jinwoo Lee, Hongwen Huang, and the other, anonymous, reviewer for their contribution to the peer review of this work. A peer review file is available.

**Reprints and permissions information** is available at <http://www.nature.com/reprints>

**Publisher's note** Springer Nature remains neutral with regard to jurisdictional claims in published maps and institutional affiliations.

**Open Access** This article is licensed under a Creative Commons Attribution-NonCommercial-NoDerivatives 4.0 International License, which permits any non-commercial use, sharing, distribution and reproduction in any medium or format, as long as you give appropriate credit to the original author(s) and the source, provide a link to the Creative Commons licence, and indicate if you modified the licensed material. You do not have permission under this licence to share adapted material derived from this article or parts of it. The images or other third party material in this article are included in the article's Creative Commons licence, unless indicated otherwise in a credit line to the material. If material is not included in the article's Creative Commons licence and your intended use is not permitted by statutory regulation or exceeds the permitted use, you will need to obtain permission directly from the copyright holder. To view a copy of this licence, visit <http://creativecommons.org/licenses/by-nc-nd/4.0/>.

© The Author(s) 2024